Journal of Magnetic Resonance 308 (2019) 106518

Contents lists available at ScienceDirect

Journal of Magnetic Resonance

journal homepage: www.elsevier.com/locate/jmr

Perspectives on microwave coupling into cylindrical and spherical rotors with dielectric lenses for magic angle spinning dynamic nuclear polarization

Pin-Hui Chen [a,b], Chukun Gao [a], Alexander B. Barnes [a,*]

[a] Department of Chemistry, Washington University in St. Louis, St. Louis, MO 63130, USA
[b] Department of Physics, Washington University in St. Louis, St. Louis, MO 63130, USA

ARTICLE INFO

Article history:
Received 21 December 2018
Revised 3 July 2019
Accepted 5 July 2019
Available online 6 July 2019

Keywords:
Dynamic nuclear polarization
Electron decoupling
Pulsed DNP
MAS spheres
Magic angle spinning

ABSTRACT

Continuous wave dynamic nuclear polarization (DNP) increases the sensitivity of NMR, yet intense microwave fields are required to transition magic angle spinning (MAS) DNP to the time domain. Here we describe and analyze Teflon lenses for cylindrical and spherical MAS rotors that focus microwave power and increase the electron Rabi frequency, ν_{1s}. Using a commercial simulation package, we solve the Maxwell equations and determine the propagation and focusing of millimeter waves (198 GHz). We then calculate the microwave intensity in a time-independent fashion to compute the ν_{1s}. With a nominal microwave power input of 5 W, the average ν_{1s} is 0.38 MHz within a 22 μL sample volume in a 3.2 mm outer diameter (OD) cylindrical rotor without a Teflon lens. Decreasing the sample volume to 3 μL and focusing the microwave beam with a Teflon lens increases the ν_{1s} to 1.5 MHz. Microwave polarization and intensity perturbations associated with diffraction through the radiofrequency coil, losses from penetration through the rotor wall, and mechanical limitations of the separation between the lens and sample are significant challenges to improving microwave coupling in MAS DNP instrumentation. To overcome these issues, we introduce a novel focusing strategy using dielectric microwave lenses installed within spinning rotors. One such 9.5 mm OD cylindrical rotor assembly implements a Teflon focusing lens to increase the ν_{1s} to 2.7 MHz within a 2 μL sample. Further, to access high spinning frequencies while also increasing ν_{1s}, we analyze microwave coupling into MAS spheres. For 9.5 mm OD spherical rotors, we compute a ν_{1s} of 0.36 MHz within a sample volume of 161 μL, and 2.5 MHz within a 3 μL sample placed at the focal point of a novel double lens insert. We conclude with an analysis and discussion of sub-millimeter diamond spherical rotors for time domain DNP at spinning frequencies >100 kHz. Sub-millimeter spherical rotors better overlap a tightly focused microwave beam, resulting in a ν_{1s} of 2.2 MHz. Lastly, we propose that sub-millimeter dielectric spherical microwave resonators will provide a means to substantially improve electron spin control in the future.

1. Introduction

Magic angle spinning (MAS) nuclear magnetic resonance (NMR) is a powerful technique to investigate molecular structure [1–8]. However, the low sensitivity of NMR spectroscopy hinders experiments and can lead to long signal averaging times. Dynamic nuclear polarization (DNP) increases MAS-NMR sensitivity by orders of magnitude by transferring polarization from electron to nuclear spins [9–14]. Common continuous-wave (CW) DNP mechanisms include the solid effect, the cross effect, and the Overhauser effect [15]. However, CW-DNP does not perform as well at room temperature and high magnetic fields [16–22], and current limitations in microwave intensity curtail the transition of DNP from CW to pulsed regimes [23].

Time domain DNP with subsequent pulsed electron decoupling is a promising route to DNP at room temperature [24]. The integrated solid effect (ISE) [25–27], nuclear orientation via electron spin locking (NOVEL) [28–30], electron-nuclear cross-polarization (eNCP) [31,32], and time-optimized (TOP) DNP [33] are all promising time domain DNP approaches that can be implemented with readily available frequency-tunable gyrotron oscillators [23,34], and semiconductor microwave switches [35]. However, these time domain DNP experiments require a high electron Rabi frequency, ν_{1s}. For example, using the frequency-swept integrated solid effect, an ν_{1s} of 1.5 MHz yields sufficient electron spin control for time

* Corresponding author.
E-mail address: barnesab@wustl.edu (A.B. Barnes).

https://doi.org/10.1016/j.jmr.2019.07.005
1090-7807/

domain DNP [26]. We therefore set out to design and analyze instrumentation to increase the electron Rabi frequency to greater than 1.5 MHz.

Different methods to increase ν_{1s} include high-power microwave sources [36–42], and also improving microwave coupling through the use of microwave resonators [43–45] and dielectric lenses [46,47]. For instance, a cylindrical Teflon lens has been shown to increase ν_{1s} from 0.84 MHz to 0.91 MHz [46].

In addition to achieving intense microwave fields, MAS DNP instrumentation must also provide intense radiofrequency (RF) fields to control and detect nuclear spins, cryogenic cooling of samples to extend spin relaxation, and sample rotation to partially average anisotropic interactions within the spin Hamiltonian [42,48,49]. Therefore, significant challenges associated with increasing the ν_{1s} in MAS DNP experiments by improving microwave coupling to the sample include microwave diffraction through the RF coil, losses from penetration through the rotor wall, and mechanical limitations to the optimal distance between the Teflon lens and sample.

To achieve higher spinning frequencies and better couple the microwaves into the sample, we have developed spherical MAS rotors for DNP-NMR [50]. For example, we have demonstrated 9.5 mm outside diameter (OD) spherical rotors can spin stably up to 10.6 kHz at the magic angle [50]. Performing time domain DNP with electron decoupling in MAS spherical rotors will be a powerful technique to investigate biological and chemical structures [23].

High Frequency Structure Simulator (HFSS; Ansys, Canonsburg, PA), a commercially available simulation package that solves Maxwell equations, determines the propagation and focusing of millimeter waves in a time-independent fashion to compute the ν_{1s} of electron spins [24,46,51]. We employ this microwave analysis strategy to investigate Teflon lenses with different sizes and shapes of rotors to improve ν_{1s}.

2. Methods

HFSS requires incident microwave power, dielectric constants (ε), and probe geometry to accurately model microwave coupling to the sample. In our laboratory, 198 GHz microwaves are generated by custom-built gyrotrons [42] and transmitted to DNP-NMR probes [52] with a corrugated waveguide. The output power of our gyrotrons currently spans from 10 to 40 W, and transmission losses are typically 3 dB, resulting in a consistent minimum power delivery of 5 W to the probe [52].

Here we modeled the microwave input into the stator as a pure Gaussian beam with a waist of 3.175 mm and a power of 5.0 W [51]. The spinning apparatus, waveguide, and radiofrequency coil for each simulation resides inside of an air box, and with exterior interfaces defined as a radiation boundary. In other words, all of the microwave power incident on the surface of the box is transmitted to the surroundings, without any power reflecting back. Meshing of the computation voxels varies depending on the size of the structures in the simulation, with typical meshing density totaling one million voxels.

The sample in the simulations is a cryoprotecting glycerol-water frozen glass. The dielectric constant ($\varepsilon = \varepsilon_r + i\varepsilon_i$) of this matrix at 77 K and 140 GHz is 3.5 (ε_r), with a loss tangent ($\tan\delta = \varepsilon_i/\varepsilon_r$) of 0.005[46]. To model the dielectric constant at 198 GHz, we retained the real part ($\varepsilon_r = 3.5$) and scaled the imaginary part ($\varepsilon_i = 0.007$), because ε_r is expected to be mostly invariant to a frequency change of 58 GHz, and ε_i scales linearly with frequency [53,54].

The pass number, how many times HFSS calculates the same model, is typically between 15 and 25 before the calculation converges and requires approximately one day of computation on a desktop computer. We calculate the electron Rabi frequency ν_{1s} after the calculation converges.

The average ν_{1s} is calculated using the same method as described previously [46,51]. This calculation method includes conversion of laboratory frame from HFSS coordinate and volume average of the peak transverse magnetic field [51]. The following equation is used to calculate ν_{1s}:

$$\nu_{1s} = \frac{1}{2} \times \gamma_s \times \frac{\mu}{V} \int_V \sqrt{|\mathrm{H} \cdot \hat{\mathrm{x}}|^2 + |\mathrm{H} \cdot \hat{\mathrm{y}}|^2}\, dV$$

where γ_s is the gyromagnetic ratio of the electron spins, μ is permeability of free space, V is the sample volume, and H is the magnetic field.

Importantly, all of these simulations have been benchmarked with experimental data previously. For example, Nanni & Barnes et al. determined a ν_{1s} of 0.84 MHz with 5 W of 250 GHz microwave power incident on a 4 mm sapphire rotor [46]. Note, that study included a Teflon lens and metallic coating on the interior of the stator to increase microwave intensity in the sample. That Nanni & Barnes et al. study also verified the value of 0.84 MHz (with 5 W of incident microwave power) using published values of electron relaxation, and a theoretical treatment of cross effect DNP performance involving Bloch equations and electron spin saturation. In a subsequent study [51], we showed that our simulations closely matched the results of Nanni & Barnes et al. for 4 mm sapphire rotors. We also have previously employed a microwave analysis to 3.2 mm cylindrical zirconia rotors [24].

In the present study, the results shown in Fig. 1A closely match the results of these previous studies, and therefore act as an experimental verification and important benchmark for all other microwave analysis presented herein. We emphasize that the goal of this study is to improve microwave coupling to MAS samples. Even if the absolute magnitude of the electron spin Rabi frequencies is not precise, the relative improvement in microwave performance is the salient aspect of the microwave analysis presented in the following sections.

3. Results & discussion

3.1. Cylindrical rotor with a 3.2 mm OD

Components were included sequentially into the simulation geometry to analyze the effects of the RF coil and rotor on the microwave beam (Fig. 1). Fig. 1A shows a Teflon lens ($\varepsilon_r = 2.1$) focusing the microwave beam into a cylindrical 22 μL sample ($\varepsilon_r = 3.5$). This model yields an average ν_{1s} of 0.67 MHz throughout the sample. The Teflon lens is composed of a curvature end with a radius of 5 mm to focus the microwaves [46] and a cylindrical stalk to fit the lens with different geometries (waveguide, stator, 9.5 mm cylindrical or spherical rotors). The focused beam results in high microwave intensity in the middle of the sample and very low power delivery at the ends. The simulation in Fig. 1B also includes a four-turn spaced RF coil that diffracts and attenuates the microwave beam, resulting in a reduction of the average ν_{1s} to 0.59 MHz. Previously, it has been calculated that an RF coil of thin wire and a tight pitch will pass microwave power without such losses [46]. However, we have not pursued this strategy because flow dynamics from variable temperature fluid can result in mechanical instability of such weakly supported coils. Such mechanical instability can have detrimental effects on RF performance, especially with high variable temperature fluid streams required for cryogenic MAS experiments below 6 Kelvin [48].

As demonstrated by Zilm and Carroll [55], the ν_{1s} can be increased by focusing the microwave beam into small volume samples. Our microwave analysis (Fig. 1C) shows an average ν_{1s} of

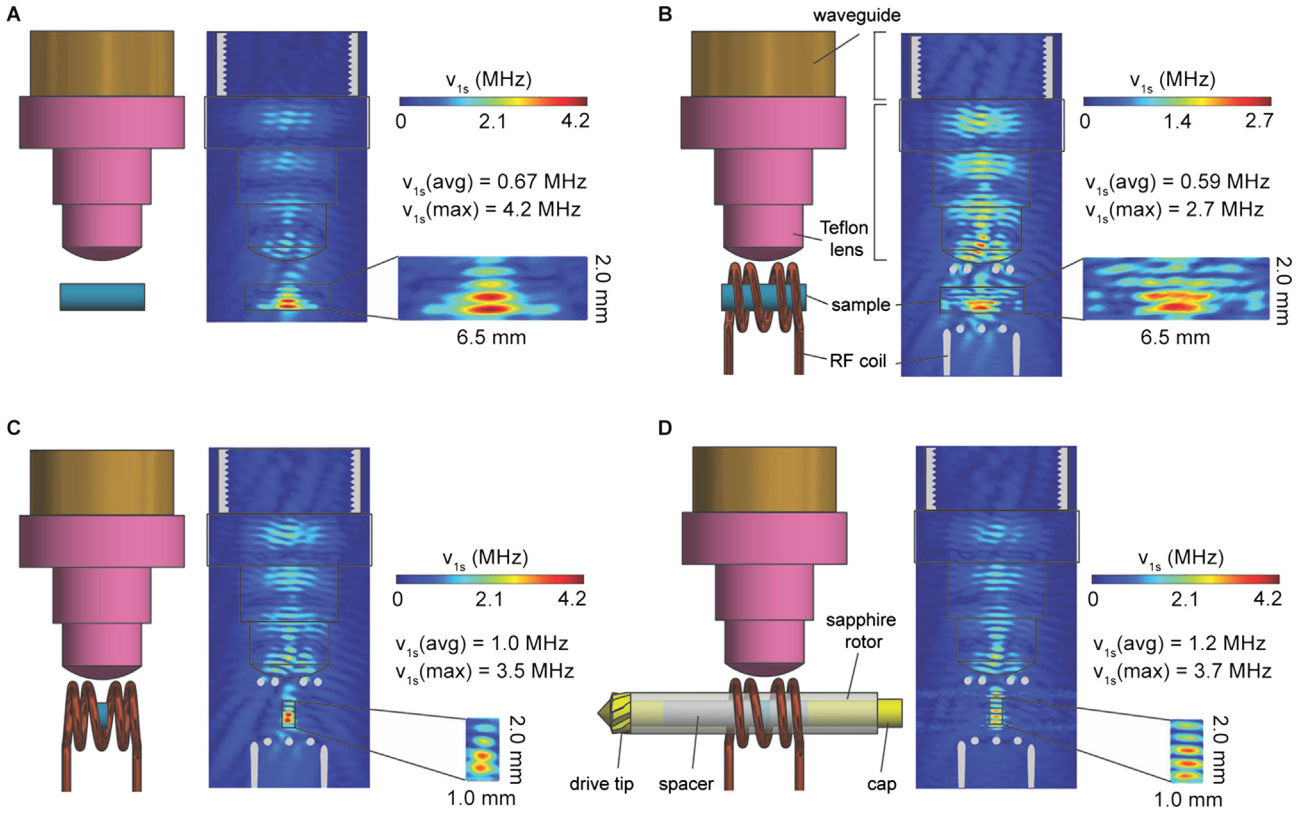

Fig. 1. HFSS results at 198 GHz with increasing system complexity. (A) Schematics and HFSS of a waveguide, Teflon focusing lens, and cryoprotected sample (~22 μL). (B) Schematics and HFSS with the addition of an RF coil. (C) Schematics and HFSS with a sample size reduction (~3 μL). (D) Schematics and HFSS results with the addition of a sapphire rotor.

1.0 MHz throughout a 3 μL sample employing this strategy. Including a cylindrical sapphire rotor results in yet additional microwave focusing into the sample, and a ν_{1s} of 1.2 MHz throughout the 3 μL sample volume (Fig. 1D).

To examine the ability of the lens to focus microwaves within the context of the complex geometry of the stator, we also performed simulations which include the Kel-F stator body and bearings (Fig. 2). Fig. 2 compares the ν_{1s} with and without the Teflon lens. Based on HFSS, the average ν_{1s} is 1.5 MHz with a Teflon lens and a small volume of 3 μL, almost four-times greater than without a Teflon lens (0.38 MHz) over a sample volume of 22 μL. We emphasize that these results compare favorably to a previous microwave analysis which has been confirmed experimentally, providing an important benchmark for our study [46]. Also note that more incident microwave power will increase ν_{1s} accordingly. Gyrotron development to generate intense microwave and frequencies suitable for high-resolution NMR is an active field of research [16,34,38,42,56]. In addition to developing higher power microwave sources (>100 kW) to perform time domain DNP on larger samples, we will also make the best use of currently available power by implementing Teflon lenses and microwave resonators.

Implementing Teflon lenses to focus power into 3.2 mm cylindrical rotors is challenged by not only diffraction through the RF coil, but also the steric hindrance of bringing the lens millimeters away from the rotor in order to maximize focusing. Therefore, we designed a 9.5 mm OD cylindrical rotor assembly that employs a Teflon lens within the rotor at the optimal distance to the sample (Fig. 3).

3.2. Cylindrical rotor with a 9.5 mm OD

Microwaves are introduced along the spinning axis in simulations of a 9.5 mm OD cylindrical rotor (Fig. 3A) [20,56]. The simulation includes the entire 9.5 mm OD cylindrical rotor, coil, waveguide, and also a thin copper disc between the drive tip and the sample for microwave reflection, which has been shown to improve DNP enhancements employing axial coupling [20,56]. Without a Teflon lens, the average simulated ν_{1s} of a 690 μL sample (ε_r = 3.5) is 0.34 MHz (Fig. 3B). Although this ν_{1s} is sufficient to generate large DNP enhancements with the cross effect, which would result in very high signal-to-noise when combined with the large sample volume, there are considerable experimental challenges to spinning 9.5 mm cylindrical rotors for cryogenic MAS DNP. For instance, spinning frequencies of 9.5 mm cylindrical rotors are limited to roughly 4 kHz and it is difficult to generate the required RF field, ν_{1I}, for proton decoupling [52]. Cryogen consumption levels for cryogenic MAS of 9.5 mm OD cylinders would also be substantial.

However, we continued to explore microwave coupling into 9.5 mm rotors with the objective of performing pulsed DNP and electron decoupling at room temperature, which would not require cryogens for MAS. We decreased the sample volume in the 9.5 mm OD cylindrical rotors (Fig. 3C), with the idea of surrounding the sample with an inductively coupled magic angle spinning coil to improve RF performance [44,57]. The spacer on the sample holder was designed such that the sample could be placed at the optimal distance for the Teflon lens to focus microwaves. We determined the optimal distance by changing the distance between the Teflon lens and the sample in HFSS (Fig. 3D–F). A lens-sample distance of 3.5 mm was found to be the optimal separation, which yields an average ν_{1s} over a 2 μL sample volume of 2.7 MHz (Fig. 3F). We note this ν_{1s} is almost eight-times greater than the ν_{1s} over 690 μL of sample in the 9.5 mm cylindrical rotor without a Teflon lens (Fig. 3B). However, we do note that maximum spinning frequency of this 9.5 mm OD cylindrical rotor apparatus is quite limited.

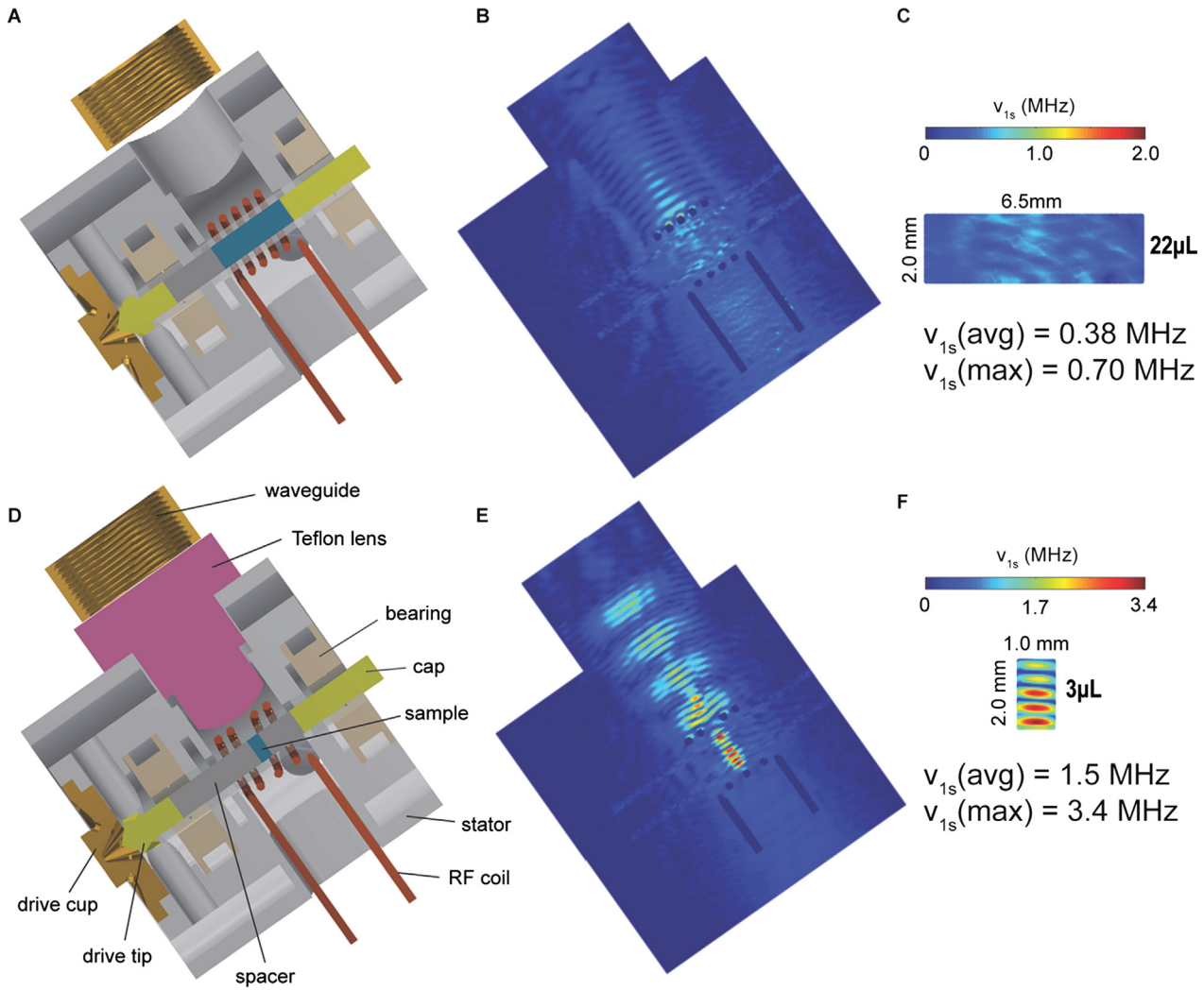

Fig. 2. Microwave analysis for 3.2 mm cylindrical rotor and stator housing. (A) Schematics for a 3.2 mm cylindrical rotor inside the MAS stator. (B) HFSS of the setup shown in (A). (C) Expansion of the sample in (B). (D) Schematics showing the installation of the Teflon focusing lens. (E) HFSS of the setup in (D). (F) Expansion of the sample in (E).

3.3. Spherical rotor with a 9.5 mm OD

In order to access higher spinning frequencies and improve MAS instrumentation, we have recently introduced MAS spherical rotors [50]. Whereas 9.5 mm OD cylindrical rotors are typically limited to 4 kHz spinning, we demonstrated 9.5 mm OD spherical rotors spinning stably at 10.6 kHz [50]. We therefore performed microwave analysis of spherical rotors. The analysis shown in Fig. 4A includes a Teflon lens within the waveguide to focus microwaves into 9.5 mm OD spherical rotors [50]. The zirconia spherical rotor ($\varepsilon_r = 20$), two polyethylene plugs ($\varepsilon_r = 2.25$), and a 161 μL sample were also included in the simulation (Fig. 4A). We found the average ν_{1s} to be 0.36 MHz over the 161 μL sample (Fig. 4B).

To improve the ν_{1s} in large volume spherical rotors, we devised a geometry which includes two Teflon lenses within the rotor (Fig. 4C). This assembly, with lenses on both spinning poles, is invariant to either orientation of the sphere with respect to the waveguide. The opposing lens also acts as a reflector to further increase the microwave intensity between the two lenses. The flat feature of the lenses on the exterior of the rotor reduces reflectance and increases microwave coupling into the spinning spheres. A Teflon lens ($\varepsilon_r = 2.1$), zirconia spherical rotor ($\varepsilon_r = 20$), interior polyethylene container ($\varepsilon_r = 2.25$), and a 3 μL sample ($\varepsilon_r = 3.5$) were included in the simulation. The average ν_{1s} is 2.5 MHz (Fig. 4D), almost seven-times greater than that in the 9.5 mm spherical rotor without the double lens insert (Fig. 4B). Although the ν_{1s} is improved to 2.5 MHz, and the filling factor of these geometries could be optimized with inductively coupled microcoils, the spinning frequency of the large 9.5 mm spherical rotors is currently limited to 10.6 kHz. Sub-millimeter spherical rotors are expected to achieve much higher spinning frequencies, and are also advantageous for microwave coupling.

3.4. Spherical rotor with a 0.5 mm OD

The focused microwave intensity in Fig. 3F shows a spherical, not cylindrical distribution, of a tightly focused microwave beam. Indeed, the cross section of tightly focused electromagnetic radiation is a circle, not a rectangle. We therefore turned to spherical samples and rotors to match the natural geometry of the microwave intensity. The sub-millimeter length scale of the spherical microwave intensity shown in Fig. 3F indicates an OD of 0.5 mm would result in effective overlap of the sample with the focused microwave beam.

We therefore turned to sub-millimeter spherical rotors to optimize microwave performance. Additionally, sub-millimeter

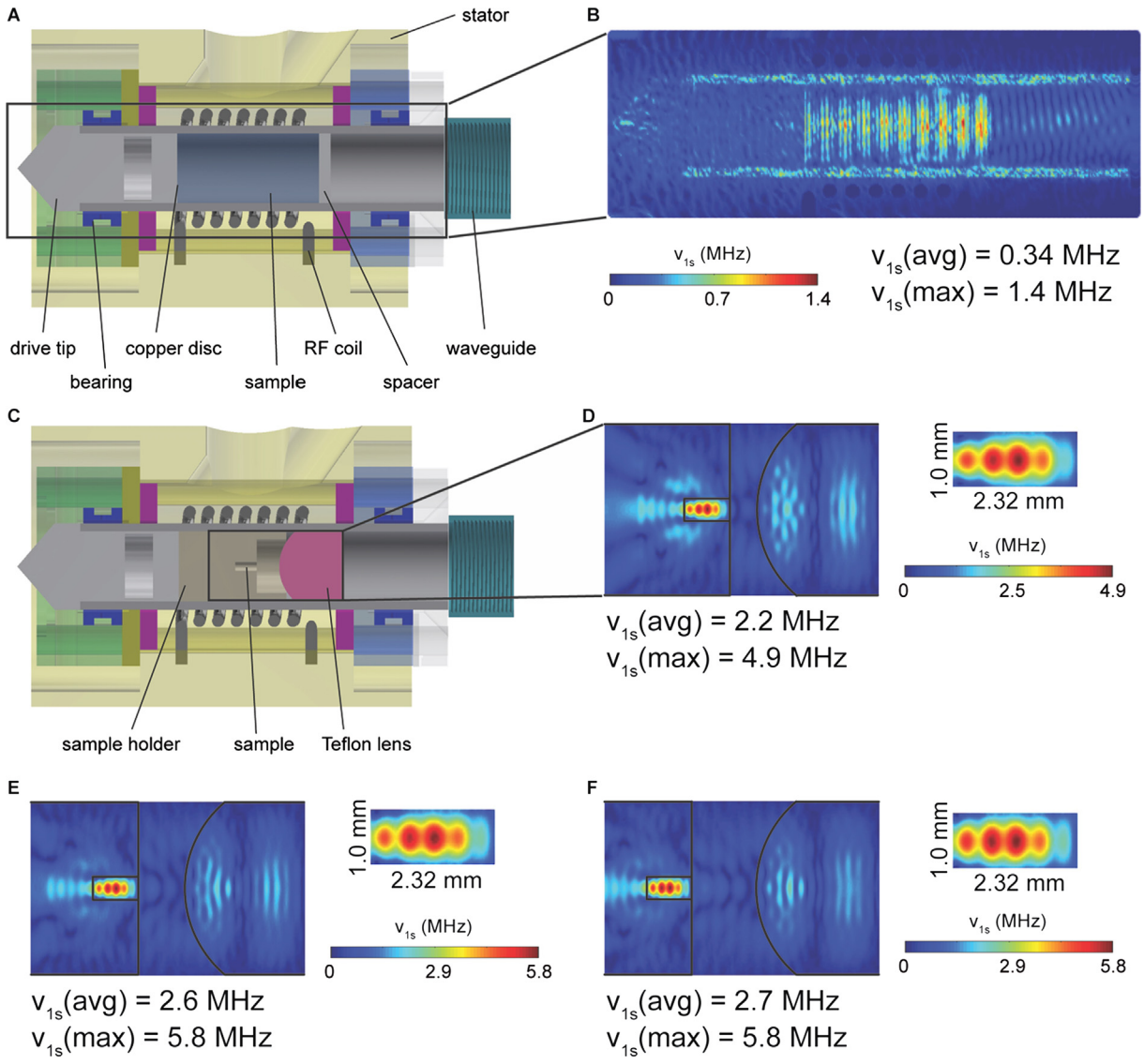

Fig. 3. Teflon lens inserted in 9.5 mm OD cylindrical rotor to focus microwave irradiation. (A) Schematics of a 9.5 OD mm cylindrical rotor inside the MAS stator. (B) HFSS of setup in the box in (A). (C) Schematics of a 9.5 mm OD cylindrical rotor, MAS stator, and Teflon focusing lens. HFSS results of the setup in the box in (C) at a distance of (D) 1.5 mm, (E) 2.5 mm, and (F) 3.5 mm. The expansions indicate the microwave intensity only of the sample.

cylindrical rotors enable spinning frequencies >110 kHz, which results in significant averaging of homonuclear proton interactions and pronounced improvements in NMR spectra [58]. The advantages of spherical rotors for MAS DNP with sub-millimeter diameters is therefore clear both in terms of electron paramagnetic resonance (EPR) performance (microwave control of electron spins) and NMR performance (spatial averaging of anisotropic interactions).

We also considered other materials for sub-millimeter spherical rotors with improved microwave transmission, thermal conduction, and mechanical strength. Yitria stabilized zirconia, sapphire, and silicon nitride are commonly employed in MAS rotors, but diamond has far superior material properties. Diamond is commonly employed in windows of megawatt gyrotrons due to both the extremely small loss tangent (5×10^{-5} at 145 GHz [59]), and also very high thermal conductivity (2400 W/m·K at 300 K, five-times higher than that of copper [59,60]). In addition to minimizing microwave losses and dissipating heat, the mechanical strength of diamond also will enable thinner rotor walls to improve sample filling factors.

In this initial investigation into spherical diamond rotors for MAS DNP, we simulate a solid 0.5 mm OD diamond sphere ($\varepsilon_r = 5.7$) (Fig. 4E). Cylindrical rotors with an OD of 0.5 mm have been successfully spun up to 126 kHz [61]. Applying MAS spheres at micron scales has considerable promise to access even higher spinning frequencies. The implementation of spherical diamond rotors for MAS will require cylindrical holes or hollowed cavities for sample loading. Due to the similar dielectric constants of diamond and glycerol-water, we expect the results shown in Fig. 4F will be generalizable to loaded spherical diamond rotors.

Microwave analysis shows an average ν_{1s} of 2.2 MHz with 5 W of microwave power (Fig. 4F). The ν_{1s} is far more homogenous in the sub-millimeter diamond sphere than larger geometries explored previously. Although adiabatic passages achieved with microwave chirped pulses are very robust to ν_{1s} inhomogeneity [46], we expect sub-millimeter sample geometries with improved ν_{1s} homogeneity to play an important role in the implementation of truly pulsed (i.e., hard pulses) EPR control with MAS. Finally, we note that sub-millimeter spherical rotors are a promising geometry for spherical dielectric microwave resonators, which could combine the advantages of microwave focusing from lenses with high quality factors.

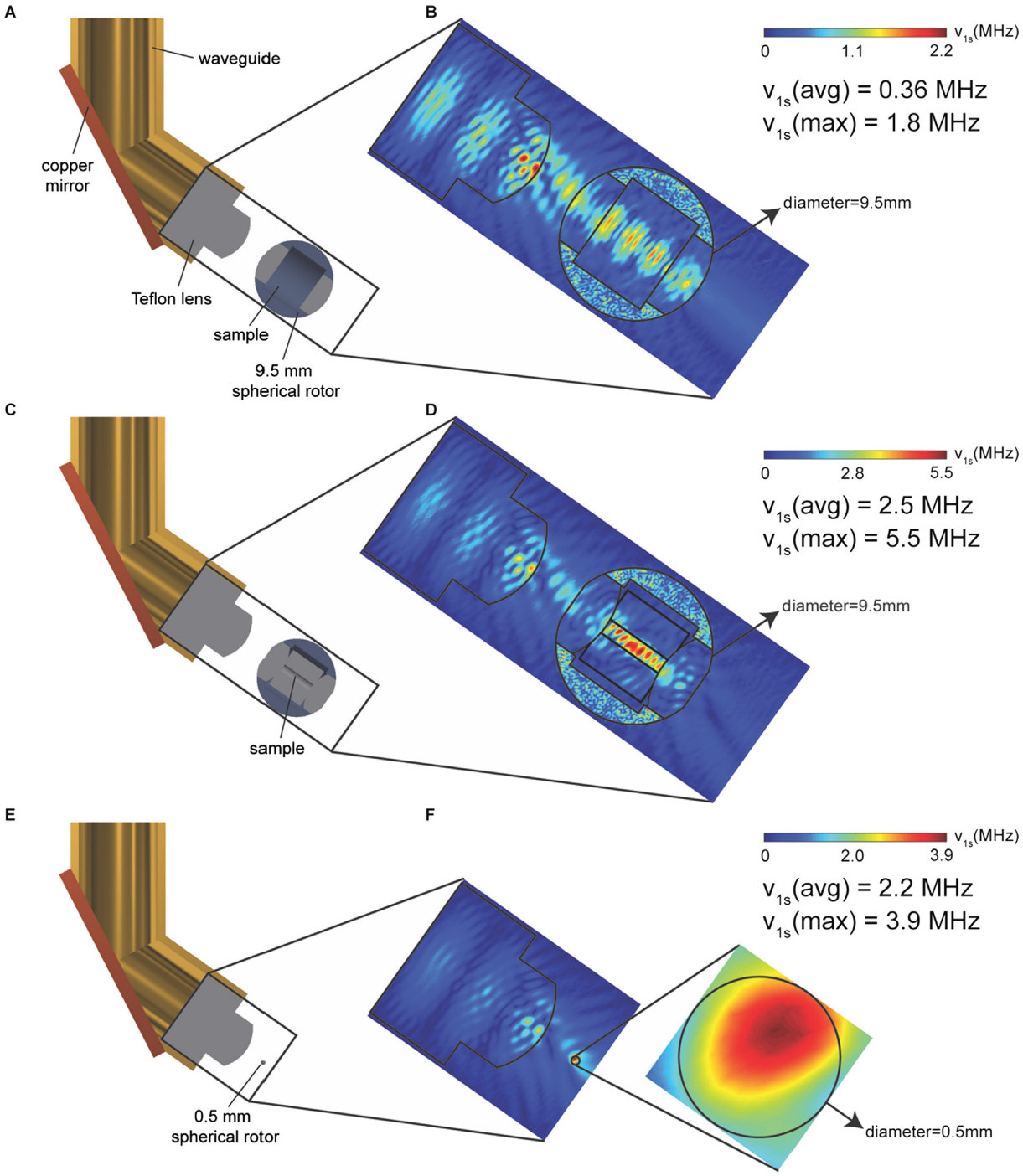

Fig. 4. Focusing microwave irradiation into spherical rotors. (A) Schematics of waveguide, Teflon lens, and 9.5 mm spherical rotor. (B) Microwave analysis of the geometry shown in (A). (C) Schematics with the addition of the double lens insert. (D) Microwave analysis of the geometry shown in (C). The double lens insert helps further focus the microwave on the sample. (E) Schematics of waveguide, Teflon lens, and 0.5 mm OD spherical rotor. (F) Microwave analysis of the geometry shown in (E).

4. Conclusions & outlook

We analyze geometries that include Teflon lenses to couple microwave power into both cylindrical and spherical rotors for MAS-DNP. HFSS was used to simulate the microwave distribution and calculate the ν_{1s}. Table 1 summarizes the ν_{1s} of the simulated geometries. The computed ν_{1s} of a 3.2 mm OD cylindrical rotor without and with a Teflon focusing lens was 0.38 MHz and 1.5 MHz, respectively. The computed ν_{1s} over 690 μL of sample within a 9.5 mm OD cylindrical rotor is 0.34 MHz, while implementing a Teflon lens increases the ν_{1s} to 2.7 MHz, albeit with a reduced sample size of 2 μL. We also analyzed 9.5 mm OD spherical rotors. The computed ν_{1s} is 0.36 MHz with a Teflon focusing lens exterior to the rotor, and 2.5 MHz with a double lens insert. A 0.5 mm OD diamond spherical rotor was also analyzed to combine advantages of high electron Rabi frequencies with high spinning frequencies. The computed ν_{1s} of the 0.5 mm OD diamond sphere was 2.2 MHz using a Teflon focusing lens.

DNP has already shown promise scaling to higher magnetic fields. For example, in addition to DNP performed at 900 MHz

Table 1
Summary of computed electron Rabi frequencies ν_{1s} with a nominal microwave power of 5 W within different MAS rotors.

	3.2 mm cylindrical rotor		9.5 mm cylindrical rotor		9.5 mm spherical rotor		0.5 mm sphere
	No Lens	Lens	No Lens	Lens	Lens	Double lens	Lens
Average ν_{1s} (MHz)	0.38	1.5	0.34	2.7	0.36	2.5	2.2
Maximum ν_{1s} (MHz)	0.70	3.4	1.4	5.8	1.8	5.5	3.9

[62], a gyrotron operating in the 2nd harmonic has already demonstrated microwave power output of 5–10 W at a frequency of 0.8 THz, suitable for DNP at 28 Tesla (1.2 GHz ^{1}H frequency) using a novel double-electron beam magnetron injection gun [63]. The microwave beam will be able to be focused to even smaller volume at higher frequencies due to the inverse scaling of wavelength. All of the microwave simulations in this study employed a nominal input of 5 W of microwave power. However, these results are general and scalable to higher microwave powers. For instance, we are currently constructing a frequency-tunable gyrotron which is modeled to produce 400 W of microwave power at 198 GHz. Assuming 3 dB loss during transmission to the probe and 200 W of incident microwave power, we expect the ν_{1s} within 0.5 mm OD diamond spheres to increase to ν_{1s} = 14 MHz. Access to such high electron Rabi frequencies is expected to play a pivotal role in the implementation of time domain DNP, improved electron decoupling, and a new suite of coherent EPR pulse sequences for MAS NMR spectroscopy.

Acknowledgments

We thank Jan Korvink, Robert Griffin, Kurt Zilm, and Kater Murch for helpful discussions. This research was supported by the NIH Director's New Innovator award number DP2GM119131, NSF CAREER award number DBI-1553577, and a Camille-Dreyfus Teacher Scholar Award.

Declaration of Competing Interest

A.B.B. and Washington University in St. Louis own intellectual property related to this work describing spinning spheres (62/703,278 filed on 25 July 2018 and 62/672,840 filed on 17 May 2018) and frequency-agile gyrotrons (US patent # US20190064088A1).

References

[1] J.S. Retel, A.J. Nieuwkoop, M. Hiller, V.A. Higman, E. Barbet-Massin, J. Stanek, L. B. Andreas, W.T. Franks, B.J. Van Rossum, K.R. Vinothkumar, L. Handel, G.G. De Palma, B. Bardiaux, G. Pintacuda, L. Emsley, W. Kühlbrandt, H. Oschkinat, Structure of outer membrane protein G in lipid bilayers, Nat. Commun. 8 (2017) 1–10, https://doi.org/10.1038/s41467-017-02228-2.
[2] M.T. Eddy, L. Andreas, O. Teijido, Y. Su, L. Clark, S.Y. Noskov, G. Wagner, T.K. Rostovtseva, R.G. Griffin, Magic angle spinning nuclear magnetic resonance characterization of voltage-dependent anion channel gating in two-dimensional lipid crystalline bilayers, Biochemistry 54 (2015) 994–1005, https://doi.org/10.1021/bi501260r.
[3] Q.Z. Ni, T.V. Can, E. Daviso, M. Belenky, R.G. Griffin, J. Herzfeld, Primary transfer step in the light-driven ion pump bacteriorhodopsin: an irreversible U-turn revealed by dynamic nuclear polarization-enhanced magic angle spinning NMR, J. Am. Chem. Soc. 140 (2018) 4085–4091, https://doi.org/10.1021/jacs.8b00022.
[4] A. McDermott, Structure and dynamics of membrane proteins by magic angle spinning solid-state NMR, Annu. Rev. Biophys. 38 (2009) 385–403, https://doi.org/10.1146/annurev.biophys.050708.133719.
[5] H. Yang, D. Staveness, S.M. Ryckbosch, A.D. Axtman, B.A. Loy, A.B. Barnes, V.S. Pande, J. Schaefer, P.A. Wender, L. Cegelski, REDOR NMR reveals multiple conformers for a protein kinase c ligand in a membrane environment, ACS Cent. Sci. 4 (2018) 89–96, https://doi.org/10.1021/acscentsci.7b00475.
[6] L.A. Baker, T. Sinnige, P. Schellenberger, J. de Keyzer, C.A. Siebert, A.J.M. Driessen, M. Baldus, K. Grünewald, Combined ^{1}H-detected solid-state NMR spectroscopy and electron cryotomography to study membrane proteins across resolutions in native environments, Structure 26 (2018) 161–170.e3, https://doi.org/10.1016/j.str.2017.11.011.
[7] M. Renault, S. Pawsey, M.P. Bos, E.J. Koers, D. Nand, R. Tommassen-, V. Boxtel, M. Rosay, J. Tommassen, W.E. Maas, M. Baldus, Solid-State NMR spectroscopy on cellular preparations enhanced by dynamic nuclear polarization **, Angew. Commun. 51 (2012) 2998–3001, https://doi.org/10.1002/anie.201105984.
[8] M. Kaplan, A. Cukkemane, G.C.P. van Zundert, S. Narasimhan, M. Daniëls, D. Mance, G. Waksman, A.M.J.J. Bonvin, R. Fronzes, G.E. Folkers, M. Baldus, Probing a cell-embedded megadalton protein complex by DNP-supported solid-state NMR, Nat. Meth. 12 (2015) 5–9, https://doi.org/10.1038/nmeth.3406.
[9] Q.Z. Ni, E. Daviso, T.V. Can, E. Markhasin, S.K. Jawla, T.M. Swager, R.J. Temkin, J. Herzfeld, R.G. Griffin, High frequency dynamic nuclear polarization, Acc. Chem. Res. 46 (2013) 1933–1941, https://doi.org/10.1021/ar300348n.
[10] A.J. Rossini, A. Zagdoun, M. Lelli, A. Lesage, C. Cop, Dynamic nuclear polarization surface enhanced NMR spectroscopy, Acc. Chem. Res. 46 (2013), https://doi.org/10.1021/ar300322x.
[11] R. Tycko, NMR at low and ultralow temperatures, Acc. Chem. Res. 46 (2013) 1923–1932, https://doi.org/10.1021/ar300358z.
[12] T. Maly, G.T. Debelouchina, V.S. Bajaj, K. Hu, C. Joo, M.L. Mak, J.R. Sirigiri, P.C.A. Van Der Wel, J. Herzfeld, R.J. Temkin, G. Robert, T. Maly, G.T. Debelouchina, V.S. Bajaj, K. Hu, C. Joo, Dynamic nuclear polarization at high magnetic fields, J. Chem. Phys. 052211 (2008), https://doi.org/10.1063/1.2833582.
[13] A.B. Barnes, G. De Paëpe, P.C.A. Van Der Wel, K.N. Hu, C.G. Joo, V.S. Bajaj, M.L. Mak-Jurkauskas, J.R. Sirigiri, J. Herzfeld, R.J. Temkin, R.G. Griffin, High-field dynamic nuclear polarization for solid and solution biological NMR, Appl. Magn. Reson. 34 (2008) 237–263, https://doi.org/10.1007/s00723-008-0129-1.
[14] T.V. Can, Q.Z. Ni, R.G. Griffin, Mechanisms of dynamic nuclear polarization in insulating solids, J. Magn. Reson. 253 (2015) 23–35, https://doi.org/10.1016/j.jmr.2015.02.005.
[15] Aany Sofia Lilly Thankamony, Johannes J. Wittmann, Monu Kaushik, Björn Corzilius, Dynamic nuclear polarization for sensitivity enhancement in modern solid-state NMR, Prog. Nucl. Magn. Reson. Spectrosc. 102-103 (2017) 120–195, https://doi.org/10.1016/j.pnmrs.2017.06.002.
[16] L.R. Becerra, G.J. Gerfen, R.J. Temkin, D.J. Singel, R.G. Griffin, Dynamic nuclear polarization with a cyclotron resonance maser at 5 T, Phys. Rev. Lett. 71 (1993) 3561–3564, https://doi.org/10.1103/PhysRevLett. 71.3561.
[17] Moreno Lelli, Sachin R. Chaudhari, David Gajan, Gilles Casano, Aaron J. Rossini, Olivier Ouari, Paul Tordo, Anne Lesage, Lyndon Emsley, Solid-state dynamic nuclear polarization at 9.4 and 18.8 T from 100 K to room temperature, J. Am. Chem. Soc. 137 (46) (2015) 14558–14561, https://doi.org/10.1021/jacs.5b08423.
[18] Ü. Akbey, W.T. Franks, A. Linden, S. Lange, R.G. Griffin, B.J. Van Rossum, H. Oschkinat, Dynamic nuclear polarization of deuterated proteins, Angew. Chem. - Int. Ed. 49 (2010) 7803–7806, https://doi.org/10.1002/anie.201002044.
[19] C. Sauvøe, M. Rosay, G. Casano, F. Aussenac, R.T. Weber, O. Ouari, P. Tordo, Highly efficient, water-soluble polarizing agents for dynamic nuclear polarization at high frequency, Angew. Chemie Int. Ed. 52 (2013) 10858–10861, https://doi.org/10.1002/anie.201304657.
[20] M. Afeworki, R.A. McKay, J. Schaefer, Dynamic nuclear polarization enhanced nuclear magnetic resonance of polymer-blend interfaces, Mater. Sci. Eng. A. 162 (1993) 221–228, https://doi.org/10.1016/0921-5093(90)90046-6.
[21] M. Afeworki, S. Vega, J. Schaefer, Direct electron-to-carbon polarization transfer in homogeneously doped polycarbonates, Macromolecules 25 (1992) 4100–4105, https://doi.org/10.1021/ma00042a009.
[22] M. Afeworki, J. Schaefer, Mechanism of DNP-enhanced polarization transfer across the interface of polycarbonate/polystyrene heterogeneous blends, Macromolecules. 25 (1992) 4092–4096, https://doi.org/10.1021/ma00042a007.
[23] E.P. Saliba, E.L. Sesti, N. Alaniva, A.B. Barnes, Pulsed electron decoupling and strategies for time domain dynamic nuclear polarization with magic angle spinning, J. Phys. Chem. Lett. 9 (2018) 5539–5547, https://doi.org/10.1021/acs.jpclett.8b01695.
[24] E.P. Saliba, E.L. Sesti, F.J. Scott, B.J. Albert, E.J. Choi, N. Alaniva, C. Gao, A.B. Barnes, Electron decoupling with dynamic nuclear polarization in rotating solids, J. Am. Chem. Soc. 139 (2017) 6310–6313, https://doi.org/10.1021/jacs.7b02714.
[25] A. Henstra, P. Dirksen, W.T. Wenckebach, Enhanced dynamic nuclear polarization by the integrated solid effect, Phys. Lett. A 134 (1988) 134–136, https://doi.org/10.1016/0375-9601(88)90950-4.
[26] T.V. Can, R.T. Weber, J.J. Walish, T.M. Swager, R.G. Griffin, Frequency-swept integrated solid effect, Angew. Chem - Int. Ed. 56 (2017) 6744–6748, https://doi.org/10.1002/anie.201700032.
[27] T.V. Can, J.E. McKay, R.T. Weber, C. Yang, T. Dubroca, J. Van Tol, S. Hill, R.G. Griffin, Frequency-swept integrated and stretched solid effect dynamic nuclear polarization, J. Phys. Chem. Lett. 9 (2018) 3187–3192, https://doi.org/10.1021/acs.jpclett.8b01002.

[28] A. Henstra, W.T. Wenckebach, The theory of nuclear orientation via electron spin locking (NOVEL), Mol. Phys. 106 (2008) 859–871, https://doi.org/10.1080/00268970801998262.
[29] T.V. Can, J.J. Walish, T.M. Swager, R.G. Griffin, Time domain DNP with the NOVEL sequence, J. Chem. Phys. 143 (2015) 1–8, https://doi.org/10.1063/1.4927087.
[30] S.K. Jain, G. Mathies, R.G. Griffin, Off-resonance NOVEL, J. Chem. Phys. 147 (2017).
[31] R. Rizzato, M. Bennati, Cross-polarization electron-nuclear double resonance spectroscopy, ChemPhysChem 16 (2015) 3769–3773, https://doi.org/10.1002/cphc.201500938.
[32] V. Weis, R.G. Griffin, Electron-nuclear cross polarization, Solid State Nucl. Magn. Reson. 29 (2006) 66–78, https://doi.org/10.1016/j.ssnmr.2005.08.005.
[33] K.O. Tan, C. Yang, R.T. Weber, G. Mathies, R.G. Griffin, Time-optimized pulsed dynamic nuclear polarization, Chem. Phys. 5 (2019) 1–8.
[34] S. Alberti, F. Braunmueller, T.M. Tran, J. Genoud, J. Hogge, M.Q. Tran, J. Ansermet, Nanosecond pulses in a THz gyrotron oscillator operating in a mode-locked self-consistent Q -switch regime, Phys. Rev. Lett. 205101 (2013) 1–5, https://doi.org/10.1103/PhysRevLett. 111.205101.
[35] S. Takahashi, L. Brunel, D.T. Edwards, J. Van Tol, G. Ramian, S. Han, M.S. Sherwin, pulsed electron paramagnetic resonance spectroscopy powered by a free-electron laser, Nature 489 (2012) 409–413, https://doi.org/10.1038/nature11437.
[36] R.G.G.V.S. Bajaj, C.T. Farrar, M.K. Hornstein, I. Mastovsky, J. Vieregg, J. Bryant, B. Elena, K.E. Kreischer, R.J. Temkin, A, Dynamic nuclear polarization at 9T using a novel 250 gyrotron microwave source, J. Magn. Reson. 160 (2003) 85–90, https://doi.org/10.1016/j.jmr.2011.08.015.
[37] A.C. Torrezan, S.T. Han, I. Mastovsky, M.A. Shapiro, J.R. Sirigiri, R.J. Temkin, A.B. Barnes, R.G. Griffin, Continuous-wave operation of a frequency-tunable 460-GHz second-harmonic gyrotron for enhanced nuclear magnetic resonance, IEEE Trans. Plasma Sci. 38 (2010) 1150–1159, https://doi.org/10.1109/TPS.2010.2046617.
[38] A.B. Barnes, E.A. Nanni, J. Herzfeld, R.G. Griffin, R.J. Temkin, A 250 GHz gyrotron with a 3 GHz tuning bandwidth for dynamic nuclear polarization, J. Magn. Reson. 221 (2012) 147–153, https://doi.org/10.1016/j.jmr.2012.03.014.
[39] S. Alberti, J.P. Ansermet, K.A. Avramides, F. Braunmueller, P. Cuanillon, J. Dubray, D. Fasel, J.P. Hogge, A. MacOr, E. De Rijk, M. Da Silva, M.Q. Tran, T.M. Tran, Q. Vuillemin, Experimental study from linear to chaotic regimes on a terahertz-frequency gyrotron oscillator, Phys. Plasmas. 19 (2012), https://doi.org/10.1063/1.4769033.
[40] D. Yoon, M. Soundararajan, P. Cuanillon, F. Braunmueller, S. Alberti, J.P. Ansermet, Dynamic nuclear polarization by frequency modulation of a tunable gyrotron of 260 GHz, J. Magn. Reson. 262 (2016) 62–67, https://doi.org/10.1016/j.jmr.2015.11.008.
[41] Y. Matsuki, T. Idehara, J. Fukazawa, T. Fujiwara, Advanced instrumentation for DNP-enhanced MAS NMR for higher magnetic fields and lower temperatures, J. Magn. Reson. 264 (2016) 107–115, https://doi.org/10.1016/j.jmr.2016.01.022.
[42] F.J. Scott, E.P. Saliba, B.J. Albert, N. Alaniva, E.L. Sesti, C. Gao, N.C. Golota, E.J. Choi, A.P. Jagtap, J.J. Wittmann, M. Eckardt, W. Harneit, B. Corzilius, S.Th. Sigurdsson, A.B. Barnes, Frequency-agile gyrotron for electron decoupling and pulsed dynamic nuclear polarization, J. Magn. Reson. 289 (2018) 45–54, https://doi.org/10.1016/j.jmr.2018.02.010.
[43] V. Denysenkov, T. Prisner, Liquid state dynamic nuclear polarization probe with fabry-perot resonator at 9.2 T, J. Magn. Reson. 217 (2012) 1–5, https://doi.org/10.1016/j.jmr.2012.01.014.
[44] S.Z. Kiss, A.M. Rostas, L. Heidinger, N. Spengler, M.V. Meissner, N. MacKinnon, E. Schleicher, S. Weber, J.G. Korvink, A microwave resonator integrated on a polymer microfluidic chip, J. Magn. Reson. 270 (2016) 169–175, https://doi.org/10.1016/j.jmr.2016.07.008.
[45] F.J. Scott, E.L. Sesti, E.J. Choi, A.J. Laut, J.R. Sirigiri, A.B. Barnes, Magic angle spinning NMR with metallized rotors as cylindrical microwave resonators, Magn. Reson. Chem. 56 (2018) 831–835, https://doi.org/10.1002/mrc.4744.
[46] E.A. Nanni, A.B. Barnes, Y. Matsuki, P.P. Woskov, B. Corzilius, R.G. Griffin, R.J. Temkin, Microwave field distribution in a magic angle spinning dynamic nuclear polarization NMR probe, J. Magn. Reson. 210 (2011) 16–23, https://doi.org/10.1016/j.jmr.2011.02.001.
[47] A. Purea, C. Reiter, A.I. Dimitriadis, E. De Rijk, F. Aussenac, I. Sergeyev, M. Rosay, F. Engelke, Improved waveguide coupling for 1. 3 mm MAS DNP probes at 263 GHz, J. Magn. Reson. 302 (2019) 43–49, https://doi.org/10.1016/j.jmr.2019.03.009.
[48] E.L. Sesti, N. Alaniva, P.W. Rand, E.J. Choi, B.J. Albert, E.P. Saliba, F.J. Scott, A.B. Barnes, Magic angle spinning NMR Below 6 K with a computational fluid dynamics analysis of fluid flow and temperature gradients, J. Magn. Reson. 286 (2017) 1–9, https://doi.org/10.1016/j.jmr.2017.11.002.
[49] I.J. Lowe, Free induction decays of rotating solids, Phys. Rev. Lett. 2 (1959) 285–287, https://doi.org/10.1103/PhysRevLett. 2.285.
[50] P. Chen, B.J. Albert, C. Gao, N. Alaniva, L.E. Price, F.J. Scott, E.P. Saliba, E.L. Sesti, P.T. Judge, E.W. Fisher, A.B. Barnes, Magic angle spinning spheres, Sci. Adv. (2018) 1–8.
[51] D.E.M. Hoff, B.J. Albert, E.P. Saliba, F.J. Scott, E.J. Choi, M. Mardini, A.B. Barnes, Frequency swept microwaves for hyperfine decoupling and time domain dynamic nuclear polarization, Solid State Nucl. Magn. Reson. 72 (2015) 79–89, https://doi.org/10.1016/j.ssnmr.2015.10.001.
[52] F.J. Scott, N. Alaniva, N.C. Golota, E.L. Sesti, E.P. Saliba, L.E. Price, B.J. Albert, P. Chen, R.D. O'Connor, A.B. Barnes, A versatile custom cryostat for dynamic nuclear polarization supports multiple cryogenic magic angle spinning transmission line probes, J. Magn. Reson. 297 (2018) 23–32, https://doi.org/10.1016/J.JMR.2018.10.002.
[53] J.H. Jiang, D.L. Wu, Ice and water permittivities for millimeter and sub-millimeter remote sensing applications, Atmos. Sci. Lett. 5 (2004) 146–151, https://doi.org/10.1002/asl.77.
[54] J. Lamb, Miscellaneous data on materials for millimetre and submillimetre optics, Int. J. Infrared Millim. Waves. 17 (1996) 1997–2034.
[55] Z.K. Carroll A., Eaton S., Eaton G., Characterizing Microwave Efficiency in DNP Instrumentation by Frequency Swept EPR, 2018.
[56] K.J. Pike, T.F. Kemp, H. Takahashi, R. Day, A.P. Howes, E.V. Kryukov, J.F. MacDonald, A.E.C. Collis, D.R. Bolton, R.J. Wylde, M. Orwick, K. Kosuga, A.J. Clark, T. Idehara, A. Watts, G.M. Smith, M.E. Newton, R. Dupree, M.E. Smith, A spectrometer designed for 6.7 and 14.1 T DNP-enhanced solid-state MAS NMR using quasi-optical microwave transmission, J. Magn. Reson. 215 (2011) 1–9, https://doi.org/10.1016/j.jmr.2011.12.006.
[57] D. Sakellariou, G. Le Goff, J.F. Jacquinot, High-resolution, high-sensitivity NMR of nanolitre anisotropic samples by coil spinning, Nature 447 (2007) 694–697, https://doi.org/10.1038/nature05897.
[58] K. Xue, R. Sarkar, C. Motz, S. Asami, V. Decker, S. Wegner, Z. Tosner, B. Reif, Magic-angle spinning frequencies beyond 300 kHz are necessary to yield maximum sensitivity in selectively methyl protonated protein samples in solid-state NMR, J. Phys. Chem. C. 122 (2018) 16437–16442, https://doi.org/10.1021/acs.jpcc.8b05600.
[59] D. Materials, The CVD diamond booklet, Online Cat (2014) 4.
[60] J.E. Graebner, in: Thermal Conductivity of Diamond BT - Diamond: Electronic Properties and Applications, Springer US, Boston, MA, 1995, pp. 285–318, https://doi.org/10.1007/978-1-4615-2257-7_7.
[61] S. Penzel, A. Oss, M. Liis, O. Ago, S. Anja, B. Matthias, E. Beat, M. Ernst, Spinning faster: protein NMR at MAS frequencies up to 126 kHz, J. Biomol. NMR (2019), https://doi.org/10.1007/s10858-018-0219-9.
[62] S. Björgvinsdóttir, B.J. Walder, A.C. Pinon, J.R. Yarava, L. Emsley, DNP enhanced NMR with flip-back recovery, J. Magn. Reson. 288 (2018) 69–75, https://doi.org/10.1016/j.jmr.2018.01.017.
[63] T. Idehara, M. Glyavin, A. Kuleshov, S. Sabchevski, T. Idehara, M. Glyavin, A. Kuleshov, S. Sabchevski, A novel THz-band double-beam gyrotron for high-field DNP-NMR spectroscopy, Rev. Sci. Instrum. 88 (2017), https://doi.org/10.1063/1.4997994.